Thermocatalytic methane pyrolysis over iron-based catalysts for turquoise hydrogen production: activity and kinetic studies

Chemical Engineering Journal 514 (2025) 163392

Contents lists available at ScienceDirect

Chemical Engineering Journal

journal homepage: www.elsevier.com/locate/cej

Thermocatalytic methane pyrolysis over iron-based catalysts for turquoise hydrogen production: activity and kinetic studies☆

Piercosimo Vedele [a], Enrico Sartoretti [a,*], Giulia Torretti [a], Chiara Novara [a], Fabio Salomone [a], Fabrizio Giorgis [a], Massimiliano Antonini [b], Samir Bensaid [a]

[a] Department of Applied Science and Technology, Politecnico di Torino, Corso Duca degli Abruzzi, 24, 10129 Turin, Italy
[b] Hysytech srl, Via I Maggio 5, 10043 Orbassano, Italy

ARTICLE INFO

Keywords:
Methane cracking
Catalytic methane pyrolysis
Turquoise hydrogen
Iron-alumina catalysts
Kinetics
Carbon nanotubes

ABSTRACT

Alumina-supported iron-based catalysts were synthesized with the aim of studying the thermocatalytic pyrolysis of methane. Two different synthesis techniques, i.e. Wet-Impregnation (WI) and Solution Combustion Synthesis (SCS), were employed to prepare samples with various formulations (40% Fe_2O_3 – 60% Al_2O_3, 60% Fe_2O_3 – 40% Al_2O_3). The structure, composition, and morphology of these materials were investigated and compared with several techniques, including inductively coupled plasma-mass spectrometry (ICP-MS), N_2-physisorption, X-ray powder diffraction (XRD), temperature programmed reduction (H_2-TPR), Raman spectroscopy, transmission and field emission scanning electron microscopy (TEM and FESEM). Time on stream and kinetic tests were carried out to evaluate the performance and kinetic parameters of the catalysts during methane decomposition. The results pointed out a higher activity and stability of the iron-based catalysts synthesized by the SCS technique and with a higher iron loading, in agreement with the calculated kinetic parameters (activation energy of 133 kJ mol^{-1} for SCS 60% Fe_2O_3 catalyst vs 160 kJ mol^{-1} for WI 60% Fe_2O_3 catalyst). The superior performance of the SCS catalysts can be attributed to an improved dispersion of iron on the alumina support. Although the SCS samples were characterized by a lower surface area, the intimate mixing of iron and alumina achieved through this technique effectively reduced the sintering of iron particles under the high temperatures encountered during both the reduction processes and the pyrolysis reaction. Furthermore, all the samples exhibited the formation of carbon nanotubes (CNTs) with varying degrees of structural order, depending on the synthesis technique and the iron loading of the catalyst.

1. Introduction

The combustion of fossil fuels to support today's energy superstructure generates large quantities of pollutants and greenhouse gases, and this issue requires urgent solutions [1]. The main source of energy is represented by hydrocarbons (71%), while only 29% of energy is derived from renewable and nuclear sources [2]. The environmental impact of the indiscriminate use of such products is rather clear, since global warming and the associated climate change are causing serious damage to populations and ecosystems. The transition from fossils to renewable sources could represent a beneficial paradigm shift. However, due to their intrinsic characteristics, wind and photovoltaic facilities introduce a misalignment between energy generation and consumption [3,4]. Consequently, it becomes imperative to substitute the combustion processes with alternative technologies that ensure a diminution in carbon emissions and, concurrently, provide programmable energy.

In this sense, hydrogen is one of the most promising energy carriers and its production represents one of the most challenging processes needed for the energetic transition towards a new greener economy. In 2022, global hydrogen consumption reached 95 Mt, with a 3% increase from the previous year. According to the "Net Zero by 2050 scenario" predicted by the International Energy Agency (IEA) [5], hydrogen use is projected to grow 6% annually, reaching over 150 Mt by 2030. The 40% of this rise will derive from new applications (heavy industry, transport, electricity generation, fuel production, etc.), different from the traditional ones (like ammonia production, refining, or chemical industry).

In this context, hydrogen exploitation allows energy production without the emission of greenhouse gases [6]. Steam Methane

☆ This article is part of a special issue entitled: 'ISCRE 28' published in Chemical Engineering Journal.

* Corresponding author.
E-mail address: enrico.sartoretti@polito.it (E. Sartoretti).

https://doi.org/10.1016/j.cej.2025.163392

Available online 5 May 2025

Reforming (SMR) (Eq. (1), coupled with Water Gas Shift (WGS) (Eq. (2), and coal gasification are the most widespread and economically advantageous techniques for hydrogen production [7]. However, these technologies are characterized by a high environmental impact in terms of global warming potential, due to their associated CO_2 emissions.

$$CH_4 + H_2O \rightarrow CO + 3H_2 \quad (1)$$

$$CO + H_2O \rightarrow CO_2 + H_2 \quad (2)$$

The implementation of CO_2 separation and sequestration processes is therefore needed [8,9]. Although the integration of carbon capture and storage (CCS) systems leads to reduced environmental impacts, the resultant net energy efficiency of the reaction drops from 75% to 60% [10]. Electrolysis based on renewable sources could represent an alternative and greener solution, thanks to the low greenhouse gases emissions. However, the high energy production cost and the strong dependence on climatic fluctuations make such technology unattractive in some contexts, at least at the moment [11,12]. Therefore, in the short/medium-term, it is necessary to develop low-cost techniques based on the exploitation of fossil fuels, but presenting a low carbon footprint.

In this sense, thermal methane decomposition (TMD), also referred to as methane pyrolysis, represents one of the most promising technologies for hydrogen production. Hydrogen produced through this technique is commonly called 'turquoise hydrogen' [13], having an intermediate environmental impact between the blue hydrogen obtained through SMR coupled with CCS and the green hydrogen from electrolysis. Methane decomposition process involves the radical dissociation mechanism of the methane molecule into hydrogen and elemental carbon (Eq. (3) [14]:

$$CH_4 \rightarrow C + 2H_2 \quad (3)$$

Despite a halved hydrogen yield with respect to SMR, methane pyrolysis ensures lower environmental impact given that no CO_2 is associated with its production. From an energetic point of view, thermal decomposition of methane is a moderately endothermic reaction [15]. The thermal energy necessary to produce a mole of molecular hydrogen is 37.8 kJ mol^{-1}, lower than the energy required by the SMR (63 kJ mol^{-1}) also considering the water vaporization enthalpy (44 kJ mol^{-1} of H_2O) [16]. This means that the methane pyrolysis process is energetically favored over the SMR reaction. Furthermore, the hydrogen production cost via TMD on an industrial scale is estimated to be between 2.6 and 3.2 € kg^{-1} (mainly depending on possible profits from the carbon product). This cost is quite comparable to the approximately 1.8 € kg^{-1} of hydrogen produced by SMR [10,17].

Due to the endothermic nature of the methane pyrolysis reaction, high temperatures (above 1000 °C) are required to achieve sufficient conversion rates [18]. The reason is ascribed to the high stability of the C-H bond and to the symmetry of the methane molecular structure [19]. However, the use of proper heterogeneous catalysts ensures an increase in the kinetics, thereby allowing to reduce the temperature at which the reaction is conducted [20]. Transition metals, like nickel, cobalt, and iron, are the most used catalysts for TMD [21,22]. Nickel catalysts are the most active ones, but they quickly deactivate above 600 °C due to the coking phenomenon [23,24]. Also, from a thermodynamic point of view, the maximum conversion at 600 °C is too low (~60%), thus implying high separation costs for the methane-hydrogen mixture in the outlet. Cobalt-based materials have similar catalytic performances, but they present higher toxicity and production costs. Iron catalysts demonstrate a lower activity compared to previous metals, but they are easily available and much less expensive. Moreover, they display an enhanced tolerance to coke-related deactivation and greater stability at elevated temperatures (700–1000 °C) [25]. This behavior is attributed to an increased carbon diffusion through the iron lattice with respect to the other metals [26,27]. A higher diffusion rate limits the deactivation of the active sites and increases the catalyst useful life. Therefore, due to their resistance characteristics, low toxicity and low cost, iron catalysts are promising candidates for the pyrolysis process on an industrial scale.

Generally, iron-based catalysts are subjected to ex-situ (calcination) and in-situ (reduction) pretreatments to obtain the methane pyrolysis active species (i.e. metallic iron). Specifically, calcination, depending on the operation temperature, can generate iron oxides in different oxidation states (hematite α-Fe_2O_3, magnetite Fe_3O_4, wustite FeO), that get reduced to metallic iron through a dedicated reducing pretratment [28]. The catalytic performances do not only depend on the nature of the metal itself, but also on the possible supports. The physico-chemical interactions between the metal and the support have a positive effect on the synthesis of metal particles possessing controlled size and good dispersion. Different materials can be used as supports, such as titania, alumina, magnesia, and silica [29–32]. The catalyst-support bond influences the dispersion and reducibility of the metal species and, consequently, their catalytic activity. A strong interaction promotes a homogeneous dispersion of the active species, preserves the surface of the metal during the reaction, and prevents the sintering of metal particles, increasing catalyst stability [33]. At the same time, a too strong interaction hinders the reduction of metal oxide, hindering the formation of active sites and affecting their catalytic activity. A proper interaction between metal species and support ensures the right balance between dispersion and reducibility of oxides. In some cases, the support can even have an active role in the catalysis. For example, Tang et al. studied the beneficial effect of ceria as iron-support on catalyst stability: they observed that the deactivation of the catalyst caused by carbon deposition was limited thanks to the partial oxidation of the deposits produced during methane pyrolysis [34]. However, SiO_2 and Al_2O_3 are the most common supports adopted for iron catalysts, thanks to a high thermal and chemical stability and a strong resistance to sintering [35,36].

In addition to the chemical composition, the synthesis technique can also influence the properties and performance of a catalyst. Wet Impregnation (WI) is widely employed for the production of catalysts, including those for methane pyrolysis: this simple technique allows precise metal loading on the support surface, but suffers from limited dispersion and sintering. Instead, different co-synthesis procedures can improve metal dispersion and stability, by promoting the intimate growth of the metal and support crystallites [37] or even the formation of solid solutions [38]. Among the co-synthesis techniques, coprecipitation, fusion and Solution Combustion Synthesis (SCS) are the most used for catalyst preparation. Co-precipitation is widely employed due to its simplicity and scalability; nevertheless, Fakeeha et al. have observed low activity during methane pyrolysis for iron-alumina catalysts obtained with this technique [28]. Fusion involves melting metal precursors at high temperatures, producing stable but low-surface-area materials [39]. SCS, on the other hand, relies on a rapid exothermic reaction between an oxidizer (e.g. metal nitrates) and a fuel (usually an organic chemical, such as urea, glycine, or citric acid) to generate highly porous catalysts with enhanced metal dispersion [40,41]. While fusion offers better thermal stability, SCS often provides superior catalytic activity due to high surface area and tunable morphology and structure, also depending on the type and quantity of fuel used during the synthesis [42,43]. In this regard, Chanoi et al have prepared $FeAlO_x$ nanocomposites by SCS using different fuels, iron loading, and heating modes [42].They found out that the type of fuel has the greatest impact on the material properties: citric acid leads to larger surface area, but the higher combustion temperature reached when using glycine allows the formation of a $FeAl_2O_4/Fe_3O_4$ solid solution, which could be expected to have better thermal stability. Indeed, the formation of hercynite ($FeAl_2O_4$) was also observed by Zhou et al., when preparing Fe–Al_2O_3 materials by fusion [39]: the presence of this phase improved catalyst stability during TMD, thanks to the strong bonding between the oxide and the active site, limiting its encapsulation by carbon [39,44]. However, although iron-alumina materials synthesized by SCS could be

promising catalysts, their application to methane pyrolysis has not yet been evaluated.

In this paper, the methane decomposition process over alumina-supported iron catalysts was investigated. The catalytic performance and kinetics of catalysts with varying iron loadings and synthesized using two different techniques (WI and SCS) were evaluated. Time on stream (TOS) tests at 800 °C were carried out to study the catalytic behavior of the samples over time. Kinetic tests allowed to assess the order of reaction and the activation energy of catalytic methane pyrolysis over these iron-alumina samples. Activity and kinetic results were correlated with the structural, morphological, and chemical characteristics of the fresh and spent materials, offering a comprehensive performance and characterization comparison between a well-established synthesis technique (WI) and an innovative one for methane pyrolysis (SCS).

2. Materials and methods

2.1. Catalyst synthesis

The present study takes into consideration two distinct synthesis techniques, i.e. Wet Impregnation and Solution Combustion Synthesis, to produce samples with different iron loadings (40 wt% Fe_2O_3 – 60 wt% Al_2O_3, 60 wt% Fe_2O_3 – 40 wt% Al_2O_3) by using alumina as support. The catalysts are designated as follows:

- Fe40Al60-WI and Fe40Al60-SCS refer to the samples consisting of 40 wt% iron oxide and 60 wt% alumina obtained through WI and SCS, respectively.
- Fe60Al40-WI and Fe60Al40-SCS refer to the samples consisting of 60 wt% iron oxide and 40 wt% alumina obtained through WI and SCS, respectively.

Wet-impregnated catalysts were prepared by adding stoichiometric amounts of $Fe(NO_3)_3{\cdot}9H_2O$ and γ-Al_2O_3 (Sigma-Aldrich) in 50 mL of de-ionized water [45]. The suspension was constantly stirred at 80 °C for 5 h until complete evaporation of water, with the aim of precipitating iron on the alumina support. The catalyst was dried at 70 °C for 14 h and finally calcined at 650 °C for 4 h with a ramp of 10 °C min^{-1}.

In the case of Solution Combustion Synthesis, stoichiometric amounts of metal precursors, i.e. $Fe(NO_3)_3{\cdot}9H_2O$ and $Al(NO_3)_3{\cdot}9H_2O$ (Sigma-Aldrich), and fuel, i.e. glycine (Alfa Aesar), were dissolved in 60 mL of de-ionized water under constant stirring for 10 min at room temperature (RT). Subsequently the solution was inserted into an oven and kept at 250 °C for 2 h (heating with a ramp of 5 °C min^{-1}) to co-synthesize the catalysts. The powder was finally calcined at 650 °C for 4 h with a ramp of 10 °C min^{-1}.

2.2. Catalyst characterization

Inductively coupled plasma-mass spectrometry (ICP-MS) was used to identify and accurately quantify the elemental composition of the catalysts. A precise mass (30 mg) of each sample was dissolved in an acid solution containing 4 mL of HNO_3, 4 mL of H_2SO_4, 2 mL of HCl and < 1 mL of HF, using an Anton Paar Multiwave 5000 microwave digestion system. The analysis was conducted through a Thermo Scientific iCAP RQ ICP-MS device.

X-ray diffraction (XRD) analysis was carried out with a Philips X'Pert PW3040 diffractometer, using Cu Kα radiation ($\lambda = 1.5418 \times 10^{-10}$ m). Scherrer's equation was applied to determine the average crystallite size, and a LaB_6 calibration standard was used to adjust for instrumental peak broadening.

The average pore properties and specific surface area (SSA) were analyzed using nitrogen physisorption with a Micromeritics Tristar II 3020 instrument, utilizing the Barrett-Joyner-Halenda (BJH) and Brunauer-Emmett-Teller (BET) methods. Before the analysis, the catalyst powder was pretreated at 200 °C for 2 h in a nitrogen (N_2) flow.

The morphology of the samples was examined using field emission scanning electron microscopy (FESEM) with a Zeiss Merlin equipped with a Gemini-II column. To enhance image quality, the solid powder was coated with a 5-nm-thick platinum (Pt) layer using sputter deposition prior to imaging.

The microstructure of the four samples was analyzed using transmission electron microscopy (TEM) with a Thermo Scientific Talos F200X microscope operating at 200 kV. The specimens were prepared by suspending the powder in 2-propanol and drop casting it on a copper grid coated with a lacey carbon film. Energy dispersive X-ray spectroscopy (EDX) was employed to collect elemental maps in scanning transmission electron microscopy (STEM) mode.

Temperature programmed reduction with hydrogen (H_2-TPR) was performed using an Altamira Ami-300Lite instrument equipped with a thermal conductivity detector (TCD). The sample powder (50 mg) was first pretreated in helium (He) at 550 °C for 30 min, then heated from 50 to 900 °C under a flow of 5% hydrogen (H_2) in argon (Ar), using a ramp of 10 °C/min.

A Renishaw InVia Raman microscope was employed to collect Raman spectra of the samples in backscattering configuration, using a 5x objective, a 514.5 nm excitation wavelength, and a 0.5 mW laser power. The RT Raman spectra were obtained averaging several spectra acquired in different regions of each sample, each one collected with a total exposure time of 225 s. The laser power was carefully adjusted in order to avoid crystallization or phase changes that may occur during the Raman measurement due the well-known sensitivity of iron oxides to laser-induced heating,

2.3. Experimental setup

All the catalytic tests were conducted in a fixed-bed reactor. The latter consists of a U-shaped quartz tube containing a catalytic bed prepared by mixing 50 mg of catalyst and 250 mg of SiO_2 as dilutant. To support and stabilize the bed, a quartz wool plug was inserted into the tube. Both the synthesis procedures produced fine powders, which would cause an increase of pressure drops and analyzer delays. Therefore, prior to the tests, the samples were pelletized and sieved to generate particles with controlled dimensions (212–300 μm). The porosity of the bed was also significantly increased by the presence of silica, leading to a reduction in pressure drops, which typically increases by the gradual deposition of solid carbon as the reaction proceeds. Temperature measurement was conducted using a K-type thermocouple placed above the catalytic bed, with the tip positioned approximately at 1 – 5 mm from it. The gas concentration analysis was performed using an ABB 2020 analyzer: hydrogen concentration was determined using a thermal conductivity detector (TCD), oxygen concentration was measured with a paramagnetic detector, while carbon monoxide, carbon dioxide and methane concentrations were quantified using an infrared detector.

Before each experiment, nitrogen was flowed into the reactor to achieve inert conditions. Prior to introducing methane, a reduction treatment was conducted. This pretreatment is necessary to reduce iron oxides, since the active species for pyrolysis is the metallic iron (Fe). The protocol involved flowing hydrogen (5% in N_2) at a rate of 120 mL min^{-1} for 130 min. This interval includes a temperature ramp from ambient to 900 °C at a rate of 10 °C min^{-1}, followed by a hold of 40 min. After the reduction process, the proper temperature was set, and methane was introduced into the reactor. Two types of tests were conducted:

- Time on stream (TOS) tests were performed to assess the catalyst deactivation over time, by introducing a specific methane concentration (3.5% CH_4 in N_2) into the reactor while maintaining the latter at a predetermined, constant temperature for several hours (800 °C for 2.5 h). The flowrate to mass ratio was maintained constant at 131

NL $g_{cat}^{-1}h^{-1}$ throughout all experiments. The residence time calculated at 800 °C varies from 0.030 to 0.031 s, depending on the bulk density of the catalyst.

- Kinetic tests were carried out by varying the methane concentration (from 3.5% to 0.5%) at a fixed temperature. Multiple tests were performed at different temperatures to evaluate the kinetic parameters of the reaction.

The main reaction conditions used during the methane pyrolysis tests are further detailed in Table 1.

3. Results and discussion

This study focuses on the characterization and performance evaluation of iron-based catalysts. The samples were synthesized with two different compositions and using two distinct procedures: Wet-Impregnation (WI) and Solution Combustion Synthesis (SCS). These methods are widely used, efficient, and cost-effective techniques for catalyst preparation, due to their simplicity and minimal waste. In WI, ferric nitrate and γ-alumina were combined in deionized water, stirred, and heated until the solvent is completely evaporated, ensuring the precipitation of iron onto alumina. The formation of metal oxides occurs primarily during the calcination phase. Instead, SCS is a co-synthesis process, involving a redox reaction between metal precursors (i.e. nitrates), and an organic fuel (i.e. glycine). The process includes mixing the precursors and the fuel in water, heating to form a gel, and then igniting it to achieve a self-propagating combustion. The high temperatures generated sustain the reaction between the oxidizer and the reducing agents, leading to the formation of a porous oxide with uniform properties.

3.1. Structural and textural properties of the fresh catalysts

Complementary characterization techniques were employed to study the surface morphology, the intrinsic structural properties, and the chemical composition of the synthesized catalysts. These properties are indeed linked to the catalytic activity of the material; hence, their knowledge enables a rigorous comparison between the various catalyst types. Preliminary studies focused on the quality of the synthesis, by evaluating the actual elemental composition of the produced samples through ICP-MS. Table 2 shows the real iron loadings of the catalysts (Fe_2O_3 wt%), which are close to the nominal values.

Nitrogen physisorption and the BET method were used to determine the specific surface area of the catalysts [46], a key parameter which is linked to the density of available active sites. The average pore diameter and total pore volume were also measured, using the BJH algorithm. Fig. 1 shows the nitrogen adsorption isotherms of all the fresh catalysts, while Table 2 presents the textural characterization results. Analysis of data obtained from nitrogen physisorption reveals significant differences in the specific surface area of the samples, depending on the composition and on the synthesis technique used. Catalysts synthesized via impregnation show higher SSA, tending to the high surface area of the alumina used as porous support (ca. 150 $m^2\ g^{-1}$). Instead, the catalysts produced via SCS, originating from iron and aluminum precursors, are characterized by lower surface area. The iron loading also significantly influences the structural characteristics of the sample. Specifically, the higher the iron loading, the lower the surface area and the pore volume. This result indicates that improved structural characteristics, in terms of surface area and porosity, can be attributed to the presence of alumina. In both WI and SCS preparation processes, the deposition of iron oxide within the cavities of alumina increases pore obstruction. This leads to a reduction in both the specific surface area and pore volume.

Table 1
Process parameters adopted during activity and stability tests performed over the synthesized catalysts.

Step	Temperature	Pressure	Gas concentration	Flow-rate	Time
	°C	bar	–	mL min^{-1}	min
Pretreatment	900	1	5% H_2	120	40
Time on stream	800	1	3.5% CH_4/N_2	120	150
Kinetics	640–720	1	0.5–3.5% CH_4/N_2	120	60

Table 2
Textural properties of the fresh iron-based catalysts.

Catalyst	Fe_2O_3 [a]	SSA [b]	V_p [b]	D_p [b]
	wt%	$m^2\ g^{-1}$	$cm^3\ g^{-1}$	nm
Fe40Al60 – WI	37.7	91.8	0.18	8.0
Fe60Al40 – WI	62.6	57.3	0.13	10.1
Fe40Al60 – SCS	40.6	46.5	0.11	9.9
Fe60Al40 – SCS	58.1	23.8	0.08	24.9
Al_2O_3	–	151	0.21	5.6

[a] The actual Fe_2O_3 content was evaluated through ICP-MS.
[b] The specific surface area (SSA), total pore volume (V_p) and average pore diameter (D_p) were measured using N_2-physisorption.

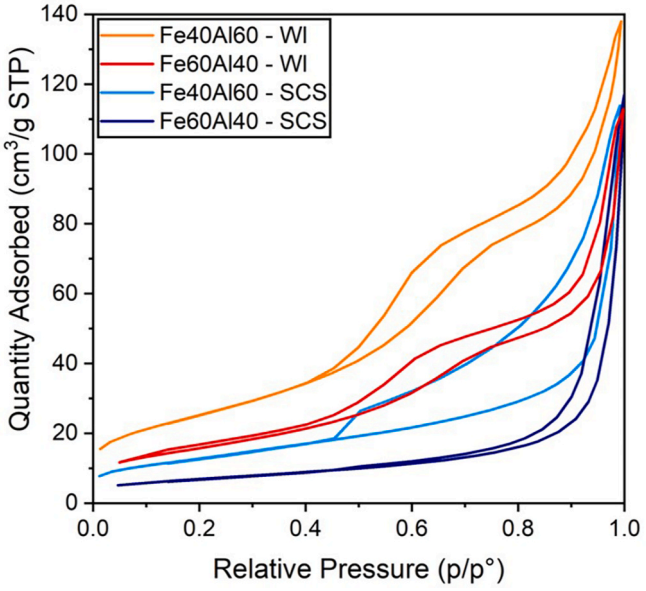

Fig. 1. Nitrogen adsorption isotherms of the fresh iron-based catalysts.

X-ray diffraction was employed to investigate the structure of the synthesized materials. Fig. 2a shows the XRD patterns of the fresh catalysts and of alumina. Analysis of the Fe40Al60 – WI and Fe60Al40 – WI profiles shows that the most intense peaks (2θ = 24.3°; 33.3°; 35.7°; 41°; 49.6°; 54.2°; 57.7°; 62.6°; 64.1°; 72.3°; 75.6°) appear in the same positions and are associated with iron oxide (α-Fe_2O_3) [47,48]. The SCS samples, and especially Fe40Al60 – SCS, exhibit a markedly different pattern from the previous ones, displaying the presence of more intense alumina peaks (in the same positions of WI fresh catalysts). Notably, this synthesis led to the formation of a mixed iron-aluminum oxide (Al_2FeO_4), with peaks observed at 2θ = 31.6°, 35.7°, 58.9°, and 64.2° [49]. Furthermore, the diffractogram associated with the Fe40Al60 – SCS catalyst is less intense compared to the others, likely due to the smaller crystallite size and a more amorphous structure.

XRD analysis has also been conducted on pretreated catalysts in order to evaluate the influence of reduction on the sample composition

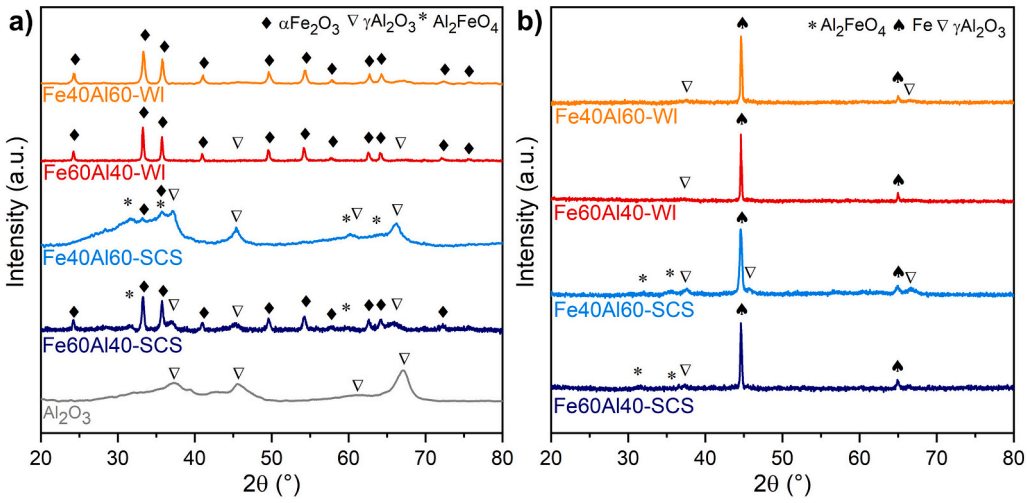

Fig. 2. Diffractograms of fresh (a) and pretreated (b) alumina-supported iron catalysts.

and structure (Fig. 2b). The formation of metallic iron as a result of the reduction process is clearly indicated by the peak at 44.6°, observed in all the diffractograms [50]. However, the Al_2FeO_4 mixed phase was still present in the SCS co-synthesized samples, even after reduction at 900 °C. Table 3 reports the crystallite size of Fe_2O_3 and metallic iron before and after the pretreatment for all the specimens. Generally, smaller crystallites were obtained through SCS synthesis. However, the crystallite diameter significantly increased after the pretreatment step, due to the coalescence of the metallic iron particles induced by the high temperature. Impregnated catalysts show not only a higher crystallite size but also a more pronounced increase. This effect can be likely attributed to a weaker interaction of iron particles with the alumina support. Conversely, the improved contact intimacy between iron and alumina in the SCS samples, which even leads to the formation of a mixed phase, helps to inhibit sintering and maintain a good iron distribution.

The structure and composition of the samples were further studied by Raman spectroscopy. Fig. 3 shows Raman spectra of the fresh iron-based catalysts. For all the analyzed samples, the detection of peaks associated with alumina is more challenging due to its relatively low degree of crystallinity. The presence of α-Fe_2O_3 (hematite) is revealed by peaks at low Raman shift values, ascribed to A_{1g} (228 cm^{-1} and 498 cm^{-1}) and E_{1g} modes (297 cm^{-1}, 414 cm^{-1}, and 612 cm^{-1}) [51–53]. The broad peak at 1350 cm^{-1} is also related to the presence of hematite [54]. A weak peak at 664 cm^{-1} suggests the existence of some Fe_3O_4 (magnetite) in the sample [55], or of structural distortion linked to the presence of defects [54]. Raman signals are particularly evident in the spectra of all the specimens except for Fe40Al60 – SCS, where peaks attributable to the main crystalline phases of iron oxide are instead absent. This is consistent with the higher degree of amorphousness exhibited by this material compared to the other catalysts, as also evidenced by the broad bands in the Raman spectrum. As Fe40Al60 – SCS, also Fe60Al40 – SCS shows a weak broad signal at 743 cm^{-1}, indicating a more amorphous structure compared to the samples obtained by impregnation.

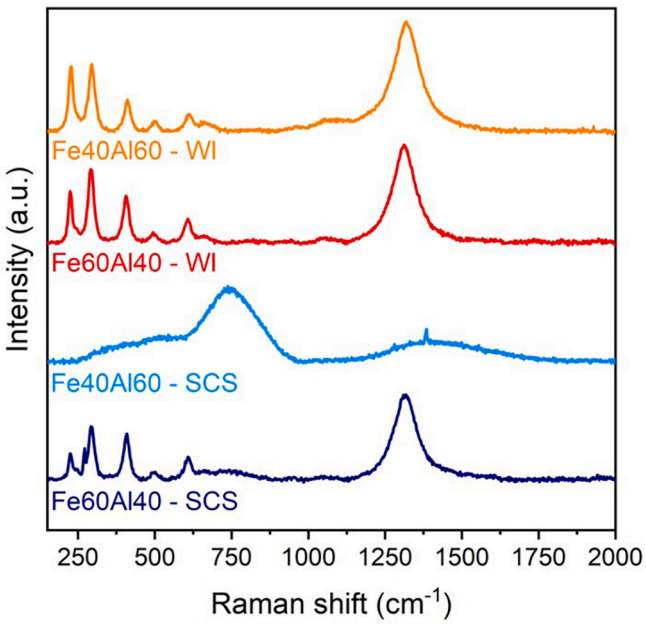

Fig. 3. Raman spectra of the fresh iron supported catalysts.

Temperature-Programmed Reduction (H_2-TPR) was further employed to investigate the reducibility of the catalysts as a function of temperature. The reduction profiles of the samples are presented in Fig. 4. The reduction process involves the passage from iron oxides, particularly Fe_2O_3, to metallic iron, which is the active site necessary for catalyzing methane pyrolysis. In analyzing the TPR profiles, distinct reduction peaks can be observed for the different catalysts. The reduction spikes at different temperatures correspond to the formation of distinct iron phases during the transition from hematite (as indicated by XRD diffractograms) to metallic iron ($Fe_2O_3 > Fe_3O_4 > FeO > Fe$). The high heating rate (10 °C min^{-1}) shifts the complete sample reduction to higher temperatures and causes overlapping of the reduction peaks observed at elevated temperatures [56]. The WI catalysts display broader and more gradual reduction peaks. This suggests a less efficient transition from Fe_2O_3 to metallic Fe, likely due to larger iron particle

Table 3
Average size of Fe_2O_3 crystallites in fresh samples and Fe crystallites in pre-reduced catalysts, estimated from XRD data using Scherrer's equation.

Catalyst	Average crystallite size[a]	
	Fe_2O_3 (fresh)	Fe (pretreated)
	nm	nm
Fe40Al60 – WI	27	99
Fe60Al40 – WI	55	139
Fe40Al60 – SCS	5	13
Fe60Al40 – SCS	29	49

[a] The average size of Fe_2O_3 crystallites in fresh samples was evaluated using the peaks at 24.3°, 33.3°, 35.7°, 41°, 49.6°, 54.2°, 62.6°, and 64.1°, while for Fe crystallites in pre-reduced catalysts the peaks at 44.6° and 64.9° were used.

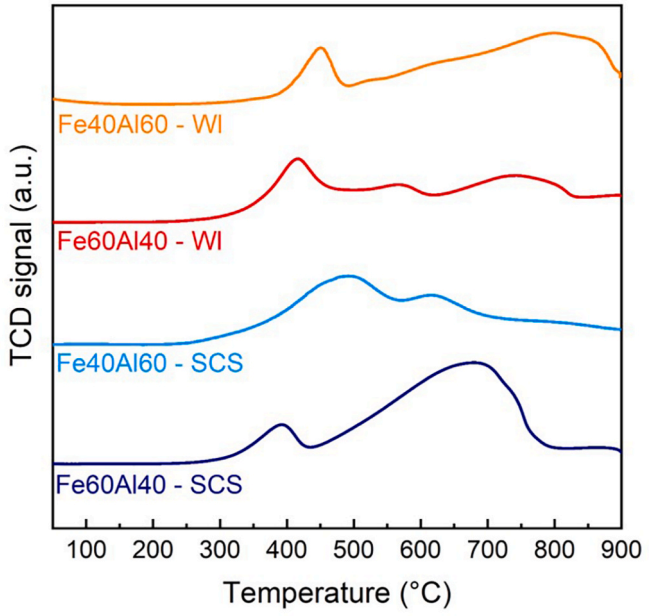

Fig. 4. Temperature-programmed reduction (H_2-TPR) profiles of the fresh iron-based catalysts.

size. In contrast, the SCS catalysts exhibit slightly more distinct reduction peaks, related to a more complete reduction process. The lower reduction temperature for the Fe60Al40 – SCS sample indicates a higher fraction of easily reducible iron oxide. This is consistent with the XRD analysis (Fig. 2b), which shows that, after the reducing pretreatment, this catalyst maintains a small crystallite size (Table 3). In fact, smaller crystallites facilitate the transition from Fe_2O_3 to metallic Fe at lower temperatures [57]. On the contrary, Fe40Al60 – SCS exhibits the first peak shifted to higher temperatures, likely due to the intimate mixing between iron and alumina, which hinders the reduction of iron oxides.

Fig. 5 shows FESEM, TEM, and STEM-EDX characterizations performed on Fe40Al60 – SCS. The FESEM image reveals the overall morphology of the catalyst, displaying irregularly shaped particles and a porous structure with a 'spongy' texture, which derives from the synthesis technique. An analogous porosity, albeit less evident, was also observed for the Fe60Al40 – SCS sample, while the WI catalysts are made of irregular rounded particles (Fig. S1). Structural features such as surface irregularities and porosity can facilitate gas diffusion during methane pyrolysis, thereby promoting catalytic activity. Fig. 5c and d present elemental distribution maps for aluminum (Al) and iron (Fe) in the Fe40Al60 – SCS sample, acquired through EDX analysis (see also Fig. S2). The uniform distribution of Al in the green map and Fe in the red map suggests effective incorporation of iron into the alumina matrix, which is critical for optimizing catalytic performance and may result from a strong metal-support interaction. Furthermore, Fig. 5e features a high-resolution transmission electron microscopy (HR-TEM) image that reveals the crystallographic structure of the catalyst. The insets highlight specific lattice planes, with measured d-spacing values of 2.02 Å for Al_2FeO_4 (400), 2.98 Å for Al_2FeO_4 (222), and 2.47 Å for Al_2FeO_4 (311), confirming the formation of a mixed iron-aluminum oxide. The Fe60Al40 – SCS catalyst showed instead the presence of small crystallites of Fe_2O_3 and Al_2O_3, but in close contact with each other, as shown in Fig. S3. Conversely, a major segregation was observed for the two WI samples, presenting big Fe_2O_3 particles surrounded by the alumina matrix (Figs. S4 and S5).

3.2. Catalytic performances

To assess the performance and long-term stability of the four samples, time on stream (TOS) tests were carried out. Prior to testing, a reduction pretreatment was conducted (5% H_2 in N_2 at 900 °C for 40 min) to convert iron oxide into metallic iron. The pyrolysis reaction was then carried out by feeding 120 mL min^{-1} of methane (3.5% CH_4 in N_2) into the reactor. All tests were conducted at 800 °C for 2.5 h. For the sake of comparison, the non-catalytic pyrolysis of methane was also performed under identical reaction conditions but filling the reactor with inert silica.

Fig. 6 presents methane conversion profiles over time for all the catalysts. The non-catalytic curve maintains a steady state throughout the entire reaction, with a conversion close to 0.5%. Instead, in the presence of the catalysts, high conversions were initially observed, followed by a quick decline and then by stabilization around a steady state. The initial rapid drop is due to a fast deactivation of most catalytic sites caused by carbon deposition. In fact, at the beginning of the reaction, the fresh catalyst has highly active Fe sites available, but they quickly transform into iron carbides (vide infra) and start being covered by the solid carbon product, causing a natural decline in conversion. Then, after 10–20 min, the conversion stabilizes, and the activity remains nearly constant throughout the test. In fact, iron carbide presents lower activity but better stability compared to metallic iron, leading to slow

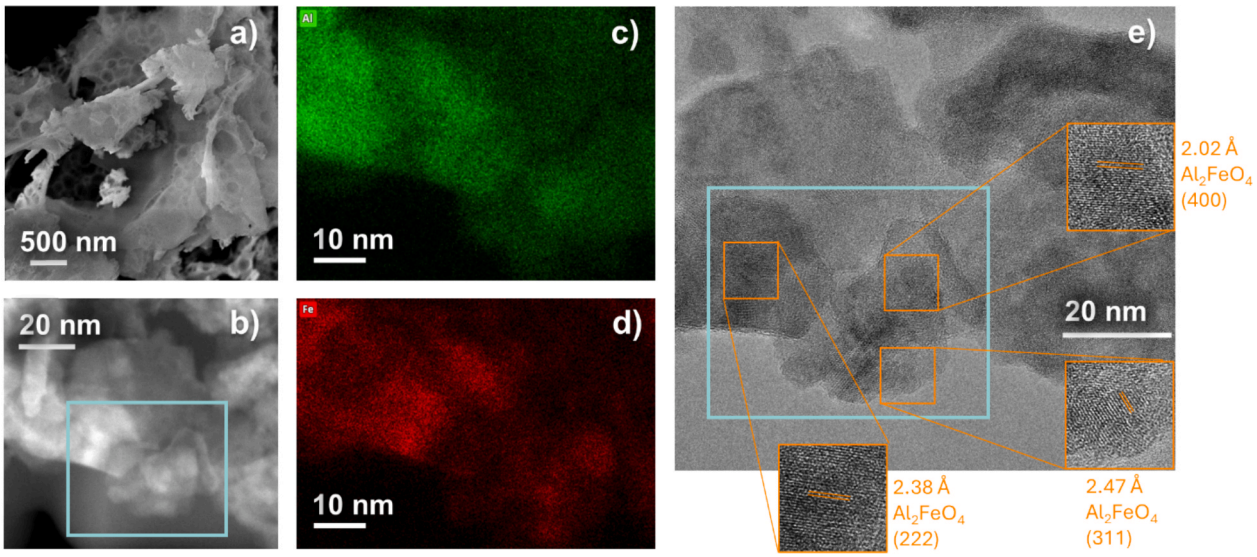

Fig. 5. Characterization of the fresh Fe40Al60 – SCS catalyst using various microscopy techniques, including FESEM (a), STEM (b), EDX (c, d) and HR-TEM (e).

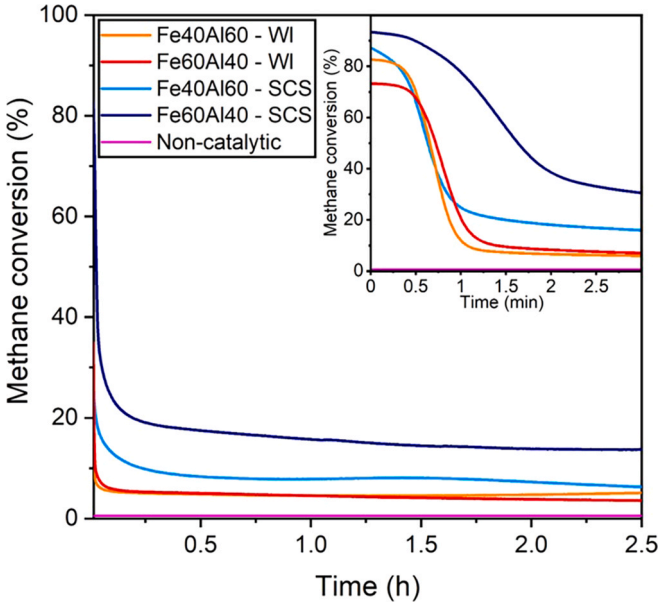

Fig. 6. Evolution of methane conversion as a function of time during TOS tests carried out at 800 °C over the iron-based catalysts. The conversion profile of non-catalytic methane decomposition is also reported for comparison.

catalyst deactivation. Additionally, an "autocatalytic" effect of the deposited carbon may contribute to maintaining a nearly constant conversion over time, since carbon nanotubes have been proven to have a certain activity for methane pyrolysis [58]. However, this contribution from CNTs can be expected to be quite marginal at 800 °C.

The conversion profiles in Fig. 6 point out a higher initial activity of the SCS samples compared to the impregnated ones, probably due to the better dispersion of small iron crystallites over the alumina matrix (as indicated by XRD and TEM results). Moreover, the SCS materials also exhibit a higher conversion plateau after the initial activity drop. This effect can be linked to the presence of Al_2FeO_4 [39]: the strong bonding between this compound and the active sites can indeed reduce sintering phenomena and hinder iron encapsulation by carbon nanotubes [59], thus improving the catalyst stability. Notably, for the SCS synthesis, the higher the iron loading, the higher the activity of the catalyst. Conversely, the two WI samples show very similar conversion curves, an indicator that an increased iron concentration from 40% to 60% does not enhance the catalytic performance of the samples obtained by impregnation. In fact, for Fe60Al40 – WI the increase in activity due to a higher iron concentration is likely offset by a reduction in specific surface area and pore volume. This phenomenon leads to an initial greater catalyst deactivation caused by carbon deposition. A brief study on the deactivation kinetics of the Fe60Al40 – WI and Fe60Al40 – SCS samples at low temperatures is reported in the Supporting Information (see Fig. S12 and Table S3). Both the catalysts show a reaction order of deactivation close to 1, but the WI sample has a quite higher activation energy for deactivation with respect to the SCS one.

3.3. Kinetic parameters

For methane pyrolysis in the absence of catalysts, activation energy values range from approximately 350 to 420 kJ mol^{-1} [60]. In order to assess how the presence of a catalyst affects this parameter, kinetic tests were carried out for the two iron-based samples with the higher iron content. This decision is driven by the aim of evaluating the kinetics of the catalyst that exhibits the best activity (Fe60Al40 – SCS) and to compare it with the catalyst with the same composition obtained through impregnation. The reaction rate for the methane pyrolysis reaction $R_{pyrolysis}$ (mol s^{-1} g^{-1}) is expressed by the following equation:

$$R_{pyrolysis} = kC_{CH_4}^{n} a(t) \quad (4)$$

where k (mol^{1-n} m^{3n} s^{-1} g^{-1}) is the kinetic constant, C_{CH4} (mol m^{-3}) is the concentration of methane, n is the order of the reaction and $a(t)$ is the time-dependent activity of the catalyst. The kinetic constant k is a function of temperature and can be derived using the Arrhenius equation:

$$k = k_{\infty} exp\left(-\frac{E_{act}}{RT}\right) \quad (5)$$

in which k_{∞} is the pre-exponential factor, E_{act} (kJ mol^{-1}) is the activation energy, R (J mol^{-1} K^{-1}) is the gas constant, and T (K) is the temperature. Values of k at various temperatures were employed to determine the pre-exponential factor and the activation energy.

The kinetic study of the catalyst was conducted at lower temperatures than that used in the TOS tests. The objective was to limit the rapid deactivation of the catalyst due to carbon deposition and to ensure that the system was operating under reaction-controlled conditions. Both phenomena would indeed contribute to the alteration of kinetic parameters. Carbon deposition leads to catalyst deactivation, resulting in an underestimation of its true activity and associated kinetic parameters. Similarly, a mass transfer-limited condition results in a reaction rate that no longer reflects the intrinsic rate of the catalyst, but is rather determined by the rate at which reactants reach the active sites. The evaluation of the rate-limiting step was carried out through a study of the Thiele modulus (the detailed procedure is described in the Supporting Information document [61]). To ensure that these phenomena did not affect the evaluation of the reaction kinetics, proper ranges of working temperatures were selected, slightly different for the two samples due to their different activity: from 660 °C to 720 °C for Fe60Al40-WI, and from 640 °C to 700 °C for Fe60Al40-SCS. At these temperatures, a weak or negligible deactivation occurred, and the system was under reaction-controlled conditions. Trials conducted at 660 °C, 690 °C, and 720 °C for the WI catalyst, as well as those at 640 °C, 665 °C, and 700 °C for the SCS sample, were repeated three times to verify the repeatability of the experiments and to enhance the accuracy of the results.

Fig. 7 illustrates the Arrhenius plot, while Table 4 presents the main parameters obtained from kinetic tests. The results confirm that the reaction order is approximately 1 (based on the averaged values obtained across all tests), which is consistent with literature data [62,63]. Moreover, the lower activation energy of the Fe60Al40-SCS sample

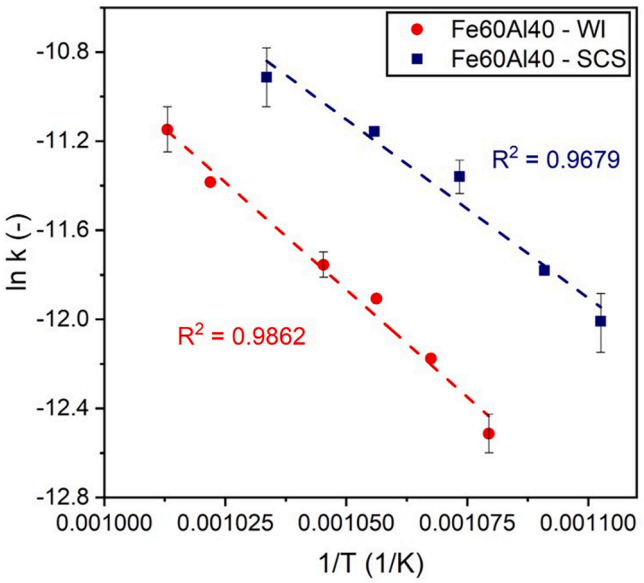

Fig. 7. Arrhenius plot of Fe60Al40 – WI and Fe60Al40 – SCS.

Table 4
Kinetic parameters of the iron-based catalysts obtained from Arrhenius plot.

Catalyst	Order of reaction n	Activation energy E_{act}	ln k_{∞} [a]
	–	kJ mol^{-1}	–
Fe60Al40 – WI	0.95	160.3 ± 9.5	8.37 ± 1.19
Fe60Al40 – SCS	1.04	133.1 ± 13.9	5.71 ± 1.80

[a] Logarithm of the pre-exponential factor.

aligns with its superior TOS performance at equivalent temperatures compared to the Fe60Al40-WI sample. The Fe60Al40 – WI catalyst shows a higher pre-exponential factor, indicating a greater concentration of active sites within the material. However, this parameter is offset by a significantly higher activation energy compared to the catalyst obtained through solution combustion synthesis. Consequently, despite having fewer active sites, the Fe60Al40 – SCS sample exhibits higher catalytic activity, as demonstrated by time on stream tests.

3.4. Structural and textural properties of the spent catalysts

A comprehensive analysis of the spent catalysts was conducted on samples tested at 800 °C for 2.5 h, in the absence of silica to avoid contamination and obtain clearer information.

A comparison of the X-ray diffractograms of fresh and spent catalysts reveals compositional changes due to the pre-reduction treatment and the deposition of graphite on the catalyst surface. As shown in Fig. 8, characteristic peaks of ferric oxide disappeared after reaction, while peaks typical of carbon appeared (2θ = 26.5°). A series of intense peaks can be observed, attributable to the presence of Fe_3C iron carbide (2θ = 37.7°, 39.7°, 40.6°, 42.8°, 43.7°, 45.9°, 48.2°, 49°, 51.7°, 54.4°, 56°, 58°, 61.4°, 70.8°, 77.8°) [57]. The formation of this compound is expected during the pyrolytic process, as it is an intermediate in the mechanism of carbon nanotube growth [64]. Also, the background noise in the diffractograms of the spent SCS samples may be linked to their lower crystallinity. Furthermore, the higher the iron loading, the clearer the XRD pattern.

A Raman investigation of the spent samples was conducted to identify the nature of the carbon formed on the surface of the catalyst during the thermocatalytic pyrolysis of methane (Fig. 9). All the analyzed

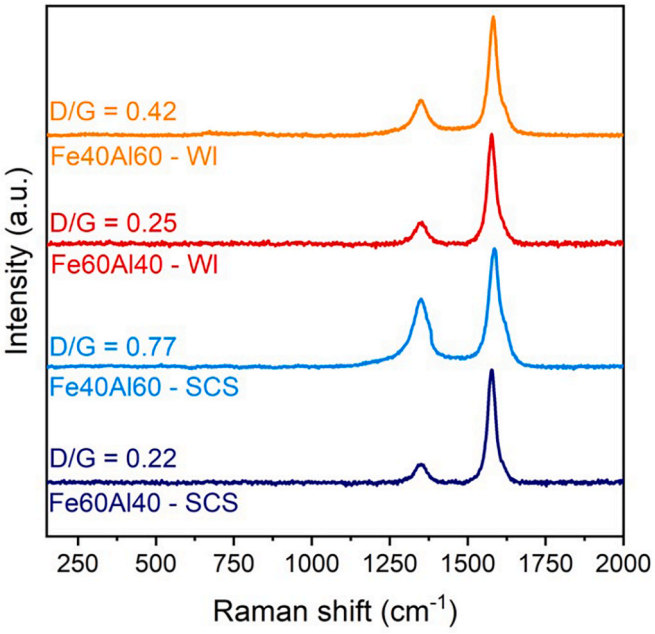

Fig. 9. Normalized Raman spectra of spent iron-based catalysts after methane pyrolysis at 800 °C for 2.5 h.

samples are characterized by an almost unperturbed peak at 1580 cm^{-1}, also referred to as the G band, that arises from the in-plane vibration of ordered sp^2 carbon atoms. An additional band at 1350 cm^{-1}, the D band, is instead characteristic of graphite with a certain degree of disorder [65–67]. The D and G bands indicate therefore the presence of a disordered and graphitic-like carbon structure, respectively, formed during the reaction. Variations in intensity and peak position reflect differences in the degree of graphitization of the carbon deposited across the catalysts. The intensity ratio between the D and G bands is hence indicative of the degree of disorder of the graphitic structure. For the catalysts with 60% iron loading, the intensity of the D band is relatively lower compared to that of Fe40Al60 samples (lower D/G ratio, see Fig. 9). This suggests that higher iron loading and larger iron particle size are

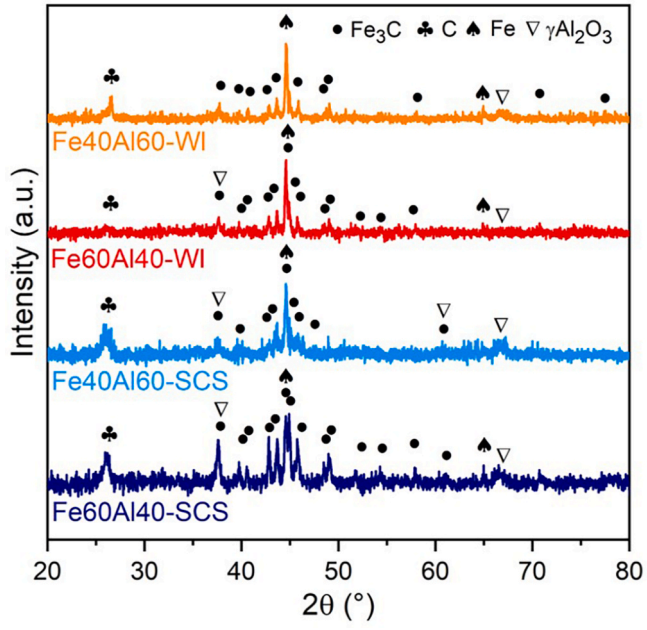

Fig. 8. X-ray diffraction patterns of spent iron-based catalysts after methane pyrolysis at 800 °C for 2.5 h.

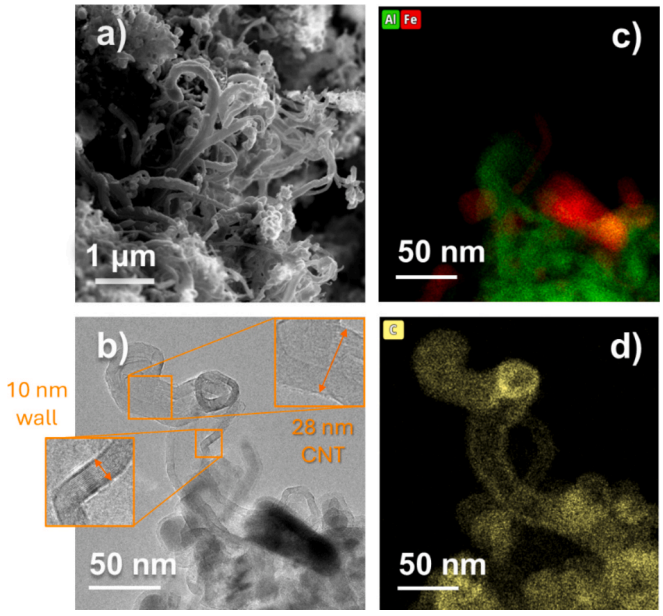

Fig. 10. FESEM (a) and TEM (b) images and STEM-EDX maps (c, d) of spent Fe40Al60-SCS catalyst after methane pyrolysis.

associated with a higher degree of order in the produced carbon.

Fig. 10 shows the characterization of the spent Fe40Al60 – SCS through FESEM, TEM and STEM-EDX. The FESEM image in Fig. 10a illustrates the overall morphology of the catalyst, highlighting the presence of elongated, tubular structures characteristic of carbon nanotubes (CNTs) emerging from the catalyst surface [68]. Fig. 10b shows a higher-resolution view obtained through TEM, which further emphasizes structural details of a nanotube. TEM analysis revealed the presence of highly crystalline multi-walled CNTs exhibiting regular fringes, characterized by interplanar spacings of about 3.27 Å. Both mechanisms of nanotube growth (i.e. base growth and tip growth [69,70]) were observed in this study, as showed by FESEM, TEM and STEM-EDX images in Supporting Information (Figs. S6–S10). Indeed, some iron particles were still in contact with the alumina support, but others were found at the tip of a CNT (see Fig. S7). Further investigations are needed to assess how these growth mechanisms influence catalyst deactivation during catalytic pyrolysis of methane. Fig. 10c displays EDX elemental maps of aluminum (Al) and iron (Fe). The overlapping regions (more abundant in the SCS samples, see Fig. S9 and S10) indicate a strong interaction between the iron catalyst and the alumina support, which is essential for maintaining catalytic activity during methane pyrolysis. Instead, more isolated iron was detected in the spent WI samples (especially in Fe60Al40 – WI, see Fig. S8), confirming their higher tendency to sintering and encapsulation of iron sites. Fig. 10d shows the distribution of carbon (in yellow), confirming the formation of carbon nanotubes in proximity to the iron sites, which play a crucial role in the dynamics of catalyst deactivation.

4. Conclusions

Methane pyrolysis is an attractive approach for hydrogen production, offering a cleaner alternative to steam reforming by avoiding the direct production of CO_2 as a byproduct. Iron-based catalysts play a crucial role in facilitating the reaction, and their performance can be influenced by the synthesis method and iron loading. In this study, the performance of four alumina-supported iron catalysts was investigated: two samples were synthesized via wet impregnation (WI) and two via solution combustion synthesis (SCS), with iron oxide loadings of 60 wt% and 40 wt% for each synthesis method. Catalysts prepared by SCS exhibit superior catalytic performance during methane pyrolysis at 800 °C, as demonstrated by time on stream tests. XRD and H_2-TPR analyses revealed that, during the pretreatment phase, all catalysts undergo the reduction of iron oxide to metallic iron, which serves as the active site for the reaction. However, while SCS catalysts maintain smaller iron crystallites and some Al_2FeO_4 mixed phase after the pretreatment, WI materials are characterized by significant coalescence of iron particles. All the samples also exhibit rapid deactivation during the initial phase of the reaction, until a steady state is reached. This behavior can be attributed to the formation of iron carbide, which has lower activity but further catalyzes the reaction, as well as the deposition of carbon nanotubes, which however might have a slight autocatalytic effect on the process. Kinetic analysis supported previous observations, showing that SCS catalysts have a lower activation energy (133 kJ mol^{-1} of Fe60Al40 – SCS compared to 160 kJ mol^{-1} of Fe60Al40 – WI catalyst) despite a lower pre-exponential factor, suggesting fewer but more active sites compared to the WI catalysts. Structural and morphological characterization of the spent catalysts using Raman spectroscopy, FESEM and TEM revealed the formation of carbon nanotubes, with both tip growth and base growth mechanisms observed. In some instances, the growth of carbon filaments led to the detachment of the iron active sites from the alumina support, in others the carbon deposits cover the active site. Overall, better iron dispersion over alumina was observed in spent SCS catalysts by EDX. These results suggest that the enhanced stability and catalytic performance of SCS materials can be attributed to better resistance to particle sintering, smaller iron crystallite size, and presence of Al_2FeO_4 mixed oxide. All these features make SCS catalysts more effective for methane pyrolysis, offering improved long-term activity and durability under reaction conditions.

CRediT authorship contribution statement

Piercosimo Vedele: Writing – review & editing, Writing – original draft, Methodology, Investigation, Formal analysis, Data curation. **Enrico Sartoretti:** Writing – review & editing, Writing – original draft, Supervision, Methodology, Investigation, Formal analysis, Data curation. **Giulia Torretti:** Investigation, Data curation. **Chiara Novara:** Writing – review & editing, Methodology. **Fabio Salomone:** Writing – review & editing, Formal analysis. **Fabrizio Giorgis:** Writing – review & editing, Resources. **Massimiliano Antonini:** Writing – review & editing, Supervision, Resources. **Samir Bensaid:** Writing – review & editing, Supervision, Resources, Funding acquisition, Formal analysis, Conceptualization.

Declaration of competing interest

The authors declare that they have no known competing financial interests or personal relationships that could have appeared to influence the work reported in this paper.

Acknowledgements

The authors kindly thank Camilla Galletti and Marco Allione for performing XRD and TEM analysis. The authors sincerely thank Alexandru Morosanu for his help during the last stages of the research study. This study was carried out within the "National Research Centre for Agricultural Technologies – AGRITECH" and received funding from the European Union Next-GenerationEU (PIANO NAZIONALE DI RIPRESA E RESILIENZA (PNRR) – MISSIONE 4 COMPONENTE 2, INVESTIMENTO 1.4 – Avviso n. 3138 del 16/12/2021, Codice Programma CN00000022). The authors also acknowledge the funding received by the Italian Ministero dell'Università e della Ricerca (MUR) under the Dipartimento di Eccellenza 2018-2022 program and the PON Ricerca e Innovazione "REACT-EU" project (DM 1062/21). This manuscript reflects only the authors' views and opinions, neither the European Union nor the European Commission can be considered responsible for them.

Appendix A. Supplementary data

Supplementary data to this article can be found online at https://doi.org/10.1016/j.cej.2025.163392.

Data availability

Data will be made available on request.

References

[1] T. Sun, I.B. Ocko, E. Sturcken, S.P. Hamburg, Path to net zero is critical to climate outcome, Sci. Rep. 11 (2021) 22173, https://doi.org/10.1038/s41598-021-01639-y.
[2] Energy Institute - Statistical Review of World Energy 2023, (n.d.).
[3] A. Pommeret, K. Schubert, Optimal energy transition with variable and intermittent renewable electricity generation, J. Econ. Dyn. Control 134 (2022) 104273, https://doi.org/10.1016/j.jedc.2021.104273.
[4] Global Hydrogen Review 2023, (2023).
[5] P.L. Joskow, Comparing the costs of intermittent and dispatchable electricity generating technologies, Am. Econ. Rev. 101 (2011) 238–241, https://doi.org/10.1257/aer.101.3.238.
[6] A. Rizzetto, E. Sartoretti, M. Piumetti, R. Pirone, S. Bensaid, Novel application of Ru-based catalysts on MgAl oxides alkaline adsorbents for cyclic CO_2 methanation, Chem. Eng. J. 501 (2024) 157585, https://doi.org/10.1016/j.cej.2024.157585.
[7] O. Machhammer, A. Bode, W. Hormuth, Financial and ecological evaluation of hydrogen production processes on large scale, Chem. Eng. Technol. 39 (2016) 1185–1193, https://doi.org/10.1002/ceat.201600023.
[8] B. Su, Y. Wang, Z. Xu, W. Han, H. Jin, H. Wang, Novel ways for hydrogen production based on methane steam and dry reforming integrated with carbon

capture, Energy Convers. Manage. 270 (2022) 116199, https://doi.org/10.1016/j.enconman.2022.116199.
[9] A. Rizzetto, M. Piumetti, R. Pirone, E. Sartoretti, S. Bensaid, Study of ceria-composite materials for high-temperature CO_2 capture and their ruthenium functionalization for methane production, Catal. Today 429 (2024) 114478, https://doi.org/10.1016/j.cattod.2023.114478.
[10] N. Sánchez-Bastardo, R. Schlögl, H. Ruland, Methane pyrolysis for zero-emission hydrogen production: a potential bridge technology from fossil fuels to a renewable and sustainable hydrogen economy, Ind. Eng. Chem. Res. 60 (2021) 11855–11881, https://doi.org/10.1021/acs.iecr.1c01679.
[11] B. Parkinson, M. Tabatabaei, D.C. Upham, B. Ballinger, C. Greig, S. Smart, E. McFarland, Hydrogen production using methane: techno-economics of decarbonizing fuels and chemicals, Int. J. Hydrogen Energy 43 (2018) 2540–2555, https://doi.org/10.1016/j.ijhydene.2017.12.081.
[12] M. Hadian, K.A. Buist, A.N.R. Bos, J.A.M. Kuipers, Single catalyst particle growth modeling in thermocatalytic decomposition of methane, Chem. Eng. J. 421 (2021) 129759, https://doi.org/10.1016/j.cej.2021.129759.
[13] J. Incer-Valverde, A. Korayem, G. Tsatsaronis, T. Morosuk, "Colors" of hydrogen: definitions and carbon intensity, Energy Convers. Manage. 291 (2023) 117294, https://doi.org/10.1016/j.enconman.2023.117294.
[14] G. Chen, X. Yu, K.(Ken) Ostrikov, B. Liu, J. Harding, G. Homm, H. Guo, S. Andreas Schunk, Y. Zhou, X. Tu, A. Weidenkaff, Methane up-carbonizing: a way towards clean hydrogen energy? Chem. Eng. J. 476 (2023) 146335 https://doi.org/10.1016/j.cej.2023.146335.
[15] F. Carretta, S. Pelucchi, F. Galli, P. Mocellin, Methane pyrolysis for hydrogen production: modeling of soot deposition by computational fluid dynamics and experimental validation, Chem. Eng. J. 485 (2024) 149844, https://doi.org/10.1016/j.cej.2024.149844.
[16] S. Schneider, S. Bajohr, F. Graf, T. Kolb, State of the art of hydrogen production via pyrolysis of natural gas, ChemBioEng Rev. 7 (2020) 150–158, https://doi.org/10.1002/cben.202000014.
[17] S. Lee, H.S. Kim, J. Park, B.M. Kang, C.-H. Cho, H. Lim, W. Won, Scenario-based techno-economic analysis of steam methane reforming process for hydrogen production, Appl. Sci. 11 (2021) 6021, https://doi.org/10.3390/app11136021.
[18] R.A. Dagle, V. Dagle, M.D. Bearden, J.D. Holladay, T.R. Krause, S. Ahmed. An Overview of Natural Gas Conversion Technologies for Co-Production of Hydrogen and Value-Added Solid Carbon Products, Pacific Northwest National Lab. (PNNL), Richland, WA (United States); Argonne National Lab. (ANL), Argonne, IL (United States), 2017. https://doi.org/10.2172/1411934.
[19] N. Muradov, Hydrogen via methane decomposition: an application for decarbonization of fossil fuels, Int. J. Hydrogen Energy 26 (2001) 1165–1175, https://doi.org/10.1016/S0360-3199(01)00073-8.
[20] T. Keipi, K.E.S. Tolvanen, H. Tolvanen, J. Konttinen, Thermo-catalytic decomposition of methane: the effect of reaction parameters on process design and the utilization possibilities of the produced carbon, Energy Convers. Manage. 126 (2016) 923–934, https://doi.org/10.1016/j.enconman.2016.08.060.
[21] N. Sánchez-Bastardo, R. Schlögl, H. Ruland, Methane pyrolysis for CO_2-free H_2 production: a green process to overcome renewable energies unsteadiness, Chem. Ing. Tech. 92 (2020) 1596–1609, https://doi.org/10.1002/cite.202000029.
[22] R.R.C.M. Silva, H.A. Oliveira, A.C.P.F. Guarino, B.B. Toledo, M.B.T. Moura, B.T. M. Oliveira, F.B. Passos, Effect of support on methane decomposition for hydrogen production over cobalt catalysts, Int. J. Hydrogen Energy 41 (2016) 6763–6772, https://doi.org/10.1016/j.ijhydene.2016.02.101.
[23] S.R. Patlolla, K. Katsu, A. Sharafian, K. Wei, O.E. Herrera, W. Mérida, A review of methane pyrolysis technologies for hydrogen production, Renew. Sustain. Energy Rev. 181 (2023) 113323, https://doi.org/10.1016/j.rser.2023.113323.
[24] U.P.M. Ashik, W.M.A. Wan Daud, H.F. Abbas, Production of greenhouse gas free hydrogen by thermocatalytic decomposition of methane – A review, Renew. Sustain. Energy Rev. 44 (2015) 221–256, https://doi.org/10.1016/j.rser.2014.12.025.
[25] M. Inaba, K. Kuramoto, Y. Soneda, Production of hydrogen and solid carbon by methane decomposition under pressurized conditions using a rotary reactor and purification of yielded hydrogen by hydrogen separation membrane, Ind. Eng. Chem. Res. 63 (2024) 4306–4316, https://doi.org/10.1021/acs.iecr.3c03696.
[26] N. Bayat, F. Meshkani, M. Rezaei, Thermocatalytic decomposition of methane to COx-free hydrogen and carbon over Ni–Fe–Cu/Al_2O_3 catalysts, Int. J. Hydrogen Energy 41 (2016) 13039–13049, https://doi.org/10.1016/j.ijhydene.2016.05.230.
[27] N. Bayat, M. Rezaei, F. Meshkani, Methane decomposition over Ni–Fe/Al_2O_3 catalysts for production of COx-free hydrogen and carbon nanofiber, Int. J. Hydrogen Energy 41 (2016) 1574–1584, https://doi.org/10.1016/j.ijhydene.2015.10.053.
[28] A.H. Fakeeha, A.A. Ibrahim, W.U. Khan, K. Seshan, R.L. Al Otaibi, A.S. Al-Fatesh, Hydrogen production via catalytic methane decomposition over alumina supported iron catalyst, Arab. J. Chem. 11 (2018) 405–414, https://doi.org/10.1016/j.arabjc.2016.06.012.
[29] M. Pudukudy, Z. Yaakob, Q. Jia, M.S. Takriff, Catalytic decomposition of methane over rare earth metal (Ce and La) oxides supported iron catalysts, Appl. Surf. Sci. 467–468 (2019) 236–248, https://doi.org/10.1016/j.apsusc.2018.10.122.
[30] W. Ahmed, M.R. Noor El-Din, A.A. Aboul-Enein, A.E. Awadallah, Effect of textural properties of alumina support on the catalytic performance of Ni/Al_2O_3 catalysts for hydrogen production via methane decomposition, J. Nat. Gas Sci. Eng. 25 (2015) 359–366, https://doi.org/10.1016/j.jngse.2015.05.015.
[31] A. Rategarpanah, F. Meshkani, Y. Wang, H. Arandiyan, M. Rezaei, Thermocatalytic conversion of methane to highly pure hydrogen over Ni–Cu/MgO·Al_2O_3 catalysts: influence of noble metals (Pt and Pd) on the catalytic activity and stability, (2018). https://doi.org/10.1016/j.enconman.2018.04.033']
[32] K. Salipira, N.J. Coville, M.S. Scurrell, Carbon produced by the catalytic decomposition of methane on nickel: carbon yields and carbon structure as a function of catalyst properties, J. Nat. Gas Sci. Eng. 32 (2016) 501–511, https://doi.org/10.1016/j.jngse.2016.04.027.
[33] A. Rastegarpanah, M. Rezaei, F. Meshkani, K. Zhang, X. Zhao, W. Pei, Y. Liu, J. Deng, H. Arandiyan, H. Dai, Mesoporous Ni/MeO (Me = Al, Mg, Ti, and Si): Highly efficient catalysts in the decomposition of methane for hydrogen production, Appl. Surf. Sci. 478 (2019) 581–593, https://doi.org/10.1016/j.apsusc.2019.02.009.
[34] L. Tang, D. Yamaguchi, N. Burke, D. Trimm, K. Chiang, Methane decomposition over ceria modified iron catalysts, Catal. Commun. 11 (2010) 1215–1219, https://doi.org/10.1016/j.catcom.2010.07.004.
[35] A.T. Mohamed, S. Ali, A. Kumar, K.C. Mondal, M.H. El-Naas, Evaluation of highly active and stable SiO_2 supported Fe-based catalysts for the catalytic methane decomposition into COx free hydrogen and CNTs, Catal. Commun. 180 (2023) 106703, https://doi.org/10.1016/j.catcom.2023.106703.
[36] S. Takenaka, M. Serizawa, K. Otsuka, Formation of filamentous carbons over supported Fe catalysts through methane decomposition, J. Catal. 222 (2004) 520–531, https://doi.org/10.1016/j.jcat.2003.11.017.
[37] M. Dosa, M.J. Marin-Figueredo, E. Sartoretti, C. Novara, F. Giorgis, S. Bensaid, D. Fino, N. Russo, M. Piumetti, Cerium-copper oxides synthesized in a multi-inlet vortex reactor as effective nanocatalysts for CO and ethene oxidation reactions, Catalysts 12 (2022) 364, https://doi.org/10.3390/catal12040364.
[38] E. Sartoretti, C. Novara, M.C. Paganini, M. Chiesa, M. Castellino, F. Giorgis, M. Piumetti, S. Bensaid, D. Fino, N. Russo, Investigation of Cu-doped ceria through a combined spectroscopic approach: involvement of different catalytic sites in CO oxidation, Catal. Today 420 (2023) 114037, https://doi.org/10.1016/j.cattod.2023.02.014.
[39] L. Zhou, L.R. Enakonda, Y. Saih, S. Loptain, D. Gary, P. Del-Gallo, J.-M. Basset, Catalytic methane decomposition over Fe-Al_2O_3, ChemSusChem 9 (2016) 1243–1248, https://doi.org/10.1002/cssc.201600310.
[40] C. Cocuzza, E. Sartoretti, C. Novara, F. Giorgis, S. Bensaid, N. Russo, D. Fino, M. Piumetti, Copper-manganese oxide catalysts prepared by solution combustion synthesis for total oxidation of VOCs, Catal. Today 423 (2023) 114292, https://doi.org/10.1016/j.cattod.2023.114292.
[41] A. Varma, A.S. Mukasyan, A.S. Rogachev, K.V. Manukyan, Solution combustion synthesis of nanoscale materials, Chem. Rev. 116 (2016) 14493–14586, https://doi.org/10.1021/acs.chemrev.6b00279.
[42] Z.A. Chanoi, V.I. Reyes, L.A. Martinez-Espinoza, E. Shafirovich, Toward a tunable fabrication of multifunctional iron-aluminum spinels via solution combustion synthesis: the effects of fuel, heating mode, and Fe:Al precursor ratio, Ceram. Int. 49 (2023) 39049–39058, https://doi.org/10.1016/j.ceramint.2023.09.242.
[43] N. Grifasi, E. Sartoretti, D. Montesi, S. Bensaid, N. Russo, F.A. Deorsola, D. Fino, C. Novara, F. Giorgis, M. Piumetti, Mesostructured manganese oxides for efficient catalytic oxidation of CO, ethylene, and propylene at mild temperatures: Insight into the role of crystalline phases and physico-chemical properties, Appl. Catal. B Environ. Energy 362 (2025) 124696, https://doi.org/10.1016/j.apcatb.2024.124696.
[44] L. Reddy Enakonda, L. Zhou, Y. Saih, S. Ould-Chikh, S. Lopatin, D. Gary, P. Del-Gallo, J. Basset, Methane-induced activation mechanism of fused ferric oxide–alumina catalysts during methane decomposition, ChemSusChem 9 (2016) 1911–1915, https://doi.org/10.1002/cssc.201600500.
[45] A.A. Ibrahim, A.H. Fakeeha, A.S. Al-Fatesh, A.E. Abasaeed, W.U. Khan, Methane decomposition over iron catalyst for hydrogen production, Int. J. Hydrogen Energy 40 (2015) 7593–7600, https://doi.org/10.1016/j.ijhydene.2014.10.058.
[46] F. Ambroz, T.J. Macdonald, V. Martis, I.P. Parkin, Evaluation of the BET theory for the characterization of meso and microporous MOFs, Small Methods 2 (2018) 1800173, https://doi.org/10.1002/smtd.201800173.
[47] J.L. Pinilla, R. Utrilla, R.K. Karn, I. Suelves, M.J. Lázaro, R. Moliner, A.B. García, J. N. Rouzaud, High temperature iron-based catalysts for hydrogen and nanostructured carbon production by methane decomposition, Int. J. Hydrogen Energy 36 (2011) 7832–7843, https://doi.org/10.1016/j.ijhydene.2011.01.184.
[48] L. Zhou, L.R. Enakonda, M. Harb, Y. Saih, A. Aguilar-Tapia, S. Ould-Chikh, J. Hazemann, J. Li, N. Wei, D. Gary, P. Del-Gallo, J.-M. Basset, Fe catalysts for methane decomposition to produce hydrogen and carbon nano materials, Appl. Catal. B Environ. 208 (2017) 44–59, https://doi.org/10.1016/j.apcatb.2017.02.052.
[49] F. Bouree, J.L. Baudour, E. Elbadraoui, J. Musso, C. Laurent, A. Rousset, Crystal and magnetic structure of piezoelectric, ferrimagnetic and magnetoelectric aluminium iron oxide $FeAlO_3$ from neutron powder diffraction, Acta Crystallogr. B 52 (1996) 217–222, https://doi.org/10.1107/S0108768195010330.
[50] I.-W. Wang, D.A. Kutteri, B. Gao, H. Tian, J. Hu, Methane pyrolysis for carbon nanotubes and CO_x -free H_2 over transition-metal catalysts, Energy Fuels 33 (2019) 197–205, https://doi.org/10.1021/acs.energyfuels.8b03502.
[51] A.C. Sparavigna. Raman Spectroscopy of the Iron Oxides in the Form of Minerals, Particles and Nanoparticles, (2023). https://doi.org/10.26434/chemrxiv-2023-22kh4-v2.
[52] Y. El Mendili, J.-F. Bardeau, N. Randrianantoandro, F. Grasset, J.-M. Greneche, Insights into the mechanism related to the phase transition from γ-Fe_2O_3 to α-Fe_2O_3 nanoparticles induced by thermal treatment and laser irradiation, J. Phys. Chem. C 116 (2012) 23785–23792, https://doi.org/10.1021/jp308418x.
[53] S.P. Schwaminger, P. Fraga-García, F. Selbach, F.G. Hein, E.C. Fuß, R. Surya, H.-C. Roth, S.A. Blank-Shim, F.E. Wagner, S. Heissler, S. Berensmeier, Bio-nano interactions: cellulase on iron oxide nanoparticle surfaces, Adsorption (2016) 1, https://doi.org/10.1007/s10450-016-9849-y.

[54] P. Krolop, A. Jantschke, S. Gilbricht, K. Niiranen, T. Seifert, Mineralogical imaging for characterization of the per Geijer apatite iron ores in the Kiruna District, Northern Sweden: a comparative study of mineral liberation analysis and Raman imaging, Minerals 9 (2019) 544, https://doi.org/10.3390/min9090544.
[55] O.N. Shebanova, P. Lazor, Raman spectroscopic study of magnetite ($FeFe_2O_4$): a new assignment for the vibrational spectrum, J. Solid State Chem. 174 (2003) 424–430, https://doi.org/10.1016/S0022-4596(03)00294-9.
[56] W.K. Jozwiak, E. Kaczmarek, T.P. Maniecki, W. Ignaczak, W. Maniukiewicz, Reduction behavior of iron oxides in hydrogen and carbon monoxide atmospheres, Appl. Catal. Gen. 326 (2007) 17–27, https://doi.org/10.1016/j.apcata.2007.03.021.
[57] E. Corrao, F. Salomone, E. Giglio, M. Castellino, S.M. Ronchetti, M. Armandi, R. Pirone, S. Bensaid, CO_2 conversion into hydrocarbons via modified Fischer-Tropsch synthesis by using bulk iron catalysts combined with zeolites, Chem. Eng. Res. Des. 197 (2023) 449–465, https://doi.org/10.1016/j.cherd.2023.07.052.
[58] D.P. Serrano, J.A. Botas, J.L.G. Fierro, R. Guil-López, P. Pizarro, G. Gómez, Hydrogen production by methane decomposition: origin of the catalytic activity of carbon materials, Fuel 89 (2010) 1241–1248, https://doi.org/10.1016/j.fuel.2009.11.030.
[59] L. Zhou, L. Li, N. Wei, J. Li, J.-M. Basset, Effect of $NiAl_2O_4$ formation on Ni/Al_2O_3 stability during dry reforming of methane, ChemCatChem 7 (2015) 2508–2516, https://doi.org/10.1002/cctc.201500379.
[60] A.I. Hussain, J. Shabanian, M. Latifi, J. Chaouki, Hydrogen production from methane thermal pyrolysis in a microwave heating-assisted fluidized bed reactor, Energy Fuels 38 (2024) 21617–21632, https://doi.org/10.1021/acs.energyfuels.4c03428.
[61] J.T. García-Sánchez, R. Valderrama-Zapata, L.F. Acevedo-Córdoba, D. Pérez-Martínez, S. Rincón-Ortiz, V.G. Baldovino-Medrano, Calculation of mass transfer limitations for a gas-phase reaction in an isothermal fixed bed reactor: tutorial and sensitivity analysis, ACS Catal. 13 (2023) 6905–6918, https://doi.org/10.1021/acscatal.3c01282.
[62] T. Becker, M. Richter, D.W. Agar, Methane pyrolysis: kinetic studies and mechanical removal of carbon deposits in reactors of different materials, Int. J. Hydrog. Energy 48 (2023) 2112–2129, https://doi.org/10.1016/j.ijhydene.2022.10.069.
[63] R. Siriwardane, J. Riley, C. Atallah, M. Bobek, Investigation of methane and ethane pyrolysis with highly active and durable iron-alumina catalyst to produce hydrogen and valuable nano carbons: continuous fluidized bed tests and reaction rate analysis, Int. J. Hydrogen Energy 48 (2023) 14210–14225, https://doi.org/10.1016/j.ijhydene.2022.12.268.
[64] A.K. Schaper, H. Hou, A. Greiner, F. Phillipp, The role of iron carbide in multiwalled carbon nanotube growth, J. Catal. 222 (2004) 250–254, https://doi.org/10.1016/j.jcat.2003.11.011.
[65] A. Jorio, M.A. Pimenta, A.G.S. Filho, R. Saito, G. Dresselhaus, M.S. Dresselhaus, Characterizing carbon nanotube samples with resonance Raman scattering, New J. Phys. 5 (2003) 139, https://doi.org/10.1088/1367-2630/5/1/139.
[66] M.S. Dresselhaus, G. Dresselhaus, R. Saito, A. Jorio. Chapter 4 Raman spectroscopy of carbon nanotubes, in: S. Saito, A. Zettl (Eds.), Contemp. Concepts Condens. Matter Sci., Elsevier, 2008: pp. 83–108. https://doi.org/10.1016/S1572-0934(08)00004-8.
[67] A. Sadezky, H. Muckenhuber, H. Grothe, R. Niessner, U. Pöschl, Raman microspectroscopy of soot and related carbonaceous materials: spectral analysis and structural information, Carbon 43 (2005) 1731–1742, https://doi.org/10.1016/j.carbon.2005.02.018.
[68] A. Naseri, E. Abbasi-Atibeh, M. Kiasadegh, J. Shen, M. Secanell, N. Semagina, J.S. Olfert. Characterization of particles generated by non-catalytic methane pyrolysis in a tubular flow reactor, Aerosol Sci. Technol. 0 (n.d.) 1–22. https://doi.org/10.1080/02786826.2024.2415486.
[69] D.A. Kutteri, I.-W. Wang, A. Samanta, L. Li, J. Hu, Methane decomposition to tip and base grown carbon nanotubes and CO_x -free H_2 over mono- and bimetallic 3d transition metal catalysts, Catal. Sci. Technol. 8 (2018) 858–869, https://doi.org/10.1039/C7CY01927K.
[70] H. Yoshida, S. Takeda, T. Uchiyama, H. Kohno, Y. Homma, Atomic-scale in-situ observation of carbon nanotube growth from solid state iron carbide nanoparticles, Nano Lett. 8 (2008) 2082–2086, https://doi.org/10.1021/nl080452q.